

# Manganese Doping Promotes the Synthesis of Bismuth-based Perovskite Nanocrystals While Tuning Their Band Structures

Maning Liu,\* Harri Ali-Löytty, Arto Hiltunen, Essi Sarlin, Syeda Qudsia, Jan-Henrik Smått, Mika Valden, and Paola Vivo\*

The doping of halide perovskite nanocrystals (NCs) with manganese cations ( $Mn^{2+}$ ) has recently enabled enhanced stability, novel optical properties, and modulated charge carrier dynamics of the NCs host. However, the influence of Mn doping on the synthetic routes and the band structures of the host has not yet been elucidated. Herein, it is demonstrated that Mn doping promotes a facile, safe, and low-hazard path toward the synthesis of ternary  $Cs_3Bi_2I_9$  NCs by effectively inhibiting the impurity phase (i.e., CsI) resulting from the decomposition of the intermediate  $Cs_3BiI_6$  product. Furthermore, it is observed that the deepening of the valence band level of the host NCs upon doping at Mn concentration levels varying from 0 to 18.5% (atomic ratio) with respect to the Bi content. As a result, the corresponding Mn-doped NCs solar cells show a higher open-circuit voltage and longer electron lifetime than those employing the undoped perovskite NCs. This work opens new insights on the role of Mn doping in the synthetic route and optoelectronic properties of lead-free halide perovskite NCs for still unexplored applications.

generally high stability, towards real optoelectronic applications.<sup>[1,2]</sup> As key representatives of lead-free perovskite NCs, bismuth (Bi)-based and antimony (Sb)-based NCs have recently been investigated with a focus on their crystal structures in the forms of vacancy-ordered double perovskites (e.g.,  $Cs_2AgBiBr_6$  and  $Cs_4CuSb_2Cl_{12}$ )<sup>[3,4]</sup> and ternary perovskites (e.g.,  $Cs_3Bi_2X_9$ , X = Cl, Br, and I).<sup>[5–7]</sup> Compared with the conventional lead-based perovskite NCs,<sup>[8]</sup> most of the lead-free perovskite NCs exhibit moderate optoelectronic properties mainly due to their featured direction-indirection transitions and low defect-tolerance, resulting in modest photoluminescence quantum yield (PLQY) and excitonic properties.<sup>[3,9,10]</sup> Impurity doping with transition-metal ions (e.g.,  $Mn^{2+}$  and  $Cu^{2+}$ ) is a known and effective way to improve the photophysical properties and stability of the host NCs due to

## 1. Introduction

All-inorganic lead-free halide perovskite nanocrystals (NCs) have attracted great attention due to their reduced toxicity and

the dopants' unique optoelectronic and magnetic properties.<sup>[11,12]</sup> The doping with Mn ions has been extensively applied to traditional semiconductor NC hosts. The explanation proposed to understand the mechanism of Mn doping includes the exciton-to-dopant energy transfer, leading to an orange emission from a spin-forbidden  $4T_1 \rightarrow {}^6A_1$  Mn d-d transition.<sup>[13,14]</sup> Recently, the success of emerging all-inorganic lead-based perovskite NCs<sup>[15,16]</sup> has extended the use of the Mn doping approach to  $CsPbX_3$  NCs.<sup>[17–20]</sup> This is also promoted by the similarity between  $Mn^{2+}$  and  $Pb^{2+}$  ionic radii and their comparable bond separation energies toward the halide anions.<sup>[21]</sup>


To date, most of the reports on Mn-doped lead-based perovskite NCs have intensively discussed the influence of Mn doping on the photoluminescence (PL)-related properties via energy transfer mechanisms, and on various stabilities of the host NCs, that is, structural, optical, and thermal.<sup>[22,23]</sup> It is well-known that the lifetime of Mn emission is on the sub-milli to millisecond time scale, which is at least more than three orders of magnitude longer than that of the excitons at the host NCs excited state (up to tens of nanoseconds).<sup>[21,24,25]</sup> In addition, the Mn doping concentration has also been reported as a key factor to influence the PLQY of the host NCs. Upon an optimal concentration of Mn doping, the surface states (e.g., defects and traps) of the host NCs can be effectively passivated by  $Mn^{2+}$  dopants, resulting in an enhanced PLQY. When doping  $Mn^{2+}$  in high concentrations, there is a possibility to observe strong  $Mn^{2+}$ - $Mn^{2+}$  interactions, which rather reduce the overall PLQY

Dr. M. Liu, Dr. A. Hiltunen, Dr. P. Vivo  
Faculty of Engineering and Natural Sciences  
Tampere University  
P.O. Box 541, Tampere FI-33014, Finland  
E-mail: maning.liu@tuni.fi; paola.vivo@tuni.fi

Dr. H. Ali-Löytty, Prof. M. Valden  
Faculty of Engineering and Natural Sciences  
Tampere University  
P.O. Box 692, Tampere FI-33014, Finland

Dr. E. Sarlin  
Faculty of Engineering and Natural Sciences  
Tampere University  
P.O. Box 589, Tampere FI-33014, Finland

S. Qudsia, Dr. J. H. Smått  
Laboratory of Molecular Science and Engineering  
Åbo Akademi University  
Porthansgatan 3–5, Turku FI-20500, Finland

 The ORCID identification number(s) for the author(s) of this article can be found under <https://doi.org/10.1002/smll.202100101>.

© 2021 The Authors. Small published by Wiley-VCH GmbH. This is an open access article under the terms of the Creative Commons Attribution License, which permits use, distribution and reproduction in any medium, provided the original work is properly cited.

DOI: 10.1002/smll.202100101

due to the excess of  $Mn^{2+}$ -induced defects allocated in the mid bandgap of the host NCs. Recently, Mn doping induced the formation of the so-called Ruddlesden-Popper defects, when  $Mn^{2+}$  ions coordinate with the lattices of the  $CsPbCl_3$  NCs, generating the quantum confinement effect within the host.<sup>[26]</sup> Despite these superior excitonic properties, Mn doping in lead-free halide perovskite NCs is still largely unexplored. In particular, to the best of our knowledge, the effect of Mn doping on the synthetic route of the host NCs has not yet been elucidated even for the widely investigated lead-based perovskite NCs. Moreover, the influence of  $Mn^{2+}$  dopants on the host NCs band structure, that is, on the tuning of the energy levels (valence band and conduction band), is currently unclear.

The synthesis of  $Cs_3Bi_2I_9$  NCs has been so far commonly carried out via hot injection, by splitting the metal halide source (e.g.,  $BiI_3$ ) into two precursors, that is,  $Bi(OAc)_3$  and trimethylsilyl iodide (TMS-I).<sup>[5,7]</sup> While this route allows to precisely control the elemental ratio between metal cations and halide anions (e.g., Cs:Bi:I), such a synthetic approach relies on the injection of a highly flammable, volatile, and corrosive compound (TMS-I) with an extremely low flash point ( $-31\text{ }^\circ\text{C}$ ). In this work, we direct the synthesis of  $Cs_3Bi_2I_9$  NCs to a high phase purity and morphological homogeneity via a safe and low-hazard hot injection route involving the addition of controlled amounts of  $Mn^{2+}$  ions that act as dopants of the host Bi-based NCs. We find that Mn doping can inhibit and even eliminate (at a high Mn concentration) the formation of CsI impurity phase originated by the decomposition of the intermediate  $Cs_3BiI_6$  product. A featured quantum confinement effect has also been observed for the Mn-doped  $Cs_3Bi_2I_9$  NCs, suggesting that Mn doping plays a relevant role in changing the size of the host NCs during the nucleation-to-growth process. The PLQY of the as-formed  $Cs_3Bi_2I_9$  NCs has been considerably improved by increasing the concentration level of Mn ions versus Bi content, due to the passivation of the surface states of the host NCs. This is also beneficial for the extension of the excitonic lifetime in the host NCs. Furthermore, we demonstrate that an increase in Mn doping amount results in the effective deepening of the valence band of  $Cs_3Bi_2I_9$  NCs, which in turn leads to an enhanced open-circuit voltage ( $V_{oc}$ ) of the corresponding solar cells and a prolonged electron lifetime on the conduction band of the electron acceptor (e.g.,  $TiO_2$ ).

## 2. Results and Discussion

### 2.1. Synthesis of Mn-doped $Cs_3Bi_2I_9$ NCs with High Phase Purity

To achieve a safe and low-hazard synthesis of  $Cs_3Bi_2I_9$  NCs, we employed the reported injection of Cs-oleate into a single metal halide source ( $BiI_3$ ), without requiring the involvement of volatile and corrosive TMS-I.<sup>[27]</sup> In this case, the  $BiI_3$  precursor simultaneously provides the source of both  $Bi^{3+}$  and  $I^-$  ions, leading to a fixed ratio (1:3) between metal cations and halide ions. Since this may not sufficiently create a halide-rich environment that is necessary for the formation of  $[BiI_6]^{3-}$  octahedra,<sup>[5]</sup> we have added  $MnI_2$  into the  $BiI_3$  precursor to tailor the concentration of iodide anions while at the same time doping the as-formed  $Cs_3Bi_2I_9$  with  $Mn^{2+}$  ions.<sup>[28,29]</sup> Since the concentration ratio between Cs

and Bi precursors (e.g.,  $r = [Cs]/[Bi]$ ) strongly influences the structure of as-formed Cs-Bi-X NCs, that is,  $Cs_3BiX_6$  ( $X = Cl, Br$ ) NCs when  $r > 1$  and  $Cs_3Bi_2X_9$  NCs ( $X = Cl, Br$  and  $I$ ) when  $r < 1$ ,<sup>[5,27]</sup> in this work we decided to focus on the latter case. It is noteworthy that a direct synthetic access to  $Cs_3BiI_6$  NCs has still not been reported, but achieved only through an anion exchange post-treatment, mainly due to the high thermodynamic instability of  $Cs_3BiI_6$  NCs during the synthesis.<sup>[7]</sup>

Monodisperse  $Cs_3Bi_2I_9$  NCs doped with  $Mn^{2+}$  (hereafter termed as  $Cs_3Bi_2I_9:Mn$ ) at nominal concentrations varying from 0 (no Mn doping) to 100 mol % were formed via a modified hot injection method (see details in the Experimental Section).<sup>[30]</sup> The actual concentration of Mn doping in  $Cs_3Bi_2I_9$  NCs suspension, determined by inductively coupled plasma mass spectroscopy (ICP-MS), showed a considerable deviation from its nominal values (Table S1, Supporting Information), as similarly observed in Mn-doped lead-based perovskite NCs.<sup>[24,28]</sup> Here, we highlight three different Mn doping weight ratios compared to the content of Bi, namely 1% (corresponding to 2.2% atomic ratio), 3% (13.7% atomic ratio), and 5% (18.5% atomic ratio) that corresponds to the limit of the Mn doping amount due to the almost saturated  $MnI_2$  in the initial precursor. It is noted that the minimum amount of Mn doping achieved in this work is 0.56% atomic ratio (see Table S1, Supporting Information), which exhibits nearly identical optical properties (data not shown) to the case of 2.2% atomic ratio. For simplicity, we thus focus on the characterization of diverse Mn-doped  $Cs_3Bi_2I_9$  NCs from the case of 1% weight ratio (2.2% atomic ratio). To determine the crystal structure of as-synthesized perovskite NCs, X-ray diffraction (XRD) patterns for perovskite NCs in film state have been acquired. **Figure 1a** shows the comparison between the XRD patterns of  $Cs_3Bi_2I_9$  without doping (reference) and with different Mn doping ratios with a complete assignment of all major featured peaks, confirming the formation of the perovskite structure. Three strong characteristic peaks at  $27.6^\circ$ ,  $39.4^\circ$ , and  $48.8^\circ$  have been observed in the pattern of  $Cs_3Bi_2I_9$  NCs without Mn doping, perfectly corresponding to the CsI structure being the main phase, according to the JCPDS reference 00-006-0311 from the ICDD database. In the meanwhile, the crystal structure of  $Cs_3Bi_2I_9$  NCs can still be determined as a second phase. Since there was no CsI reactant in the initial precursor, the generated CsI phase should necessarily be one of the products or byproducts of the reaction. In correlation with the reported decomposition of  $Cs_3BiI_6$  NCs shown in Equation (1),<sup>[7]</sup> we hypothesize that the  $Cs_3BiI_6$  NCs were initially formed after the



injection of Cs-oleate into the  $BiI_3$  precursor, then decomposed into CsI and  $Cs_3Bi_2I_9$  (the molar ratio is 3:1) due to their high thermodynamic instability. Already upon 1% Mn doping, the CsI phase is significantly reduced as evidenced by the sharp weakening of all the three characteristic peaks (e.g.,  $27.6^\circ$ ,  $39.4^\circ$ , and  $48.8^\circ$ ), meaning that the formation of initial  $Cs_3BiI_6$  NCs is effectively inhibited with the direct formation of  $Cs_3Bi_2I_9:Mn$  NCs as the major product.

With further Mn doping (e.g., >3%), the formation of the CsI phase is nearly negligible since the two characteristic peaks at  $39.4^\circ$  and  $48.8^\circ$   $2\theta$  have been reduced close to the noise

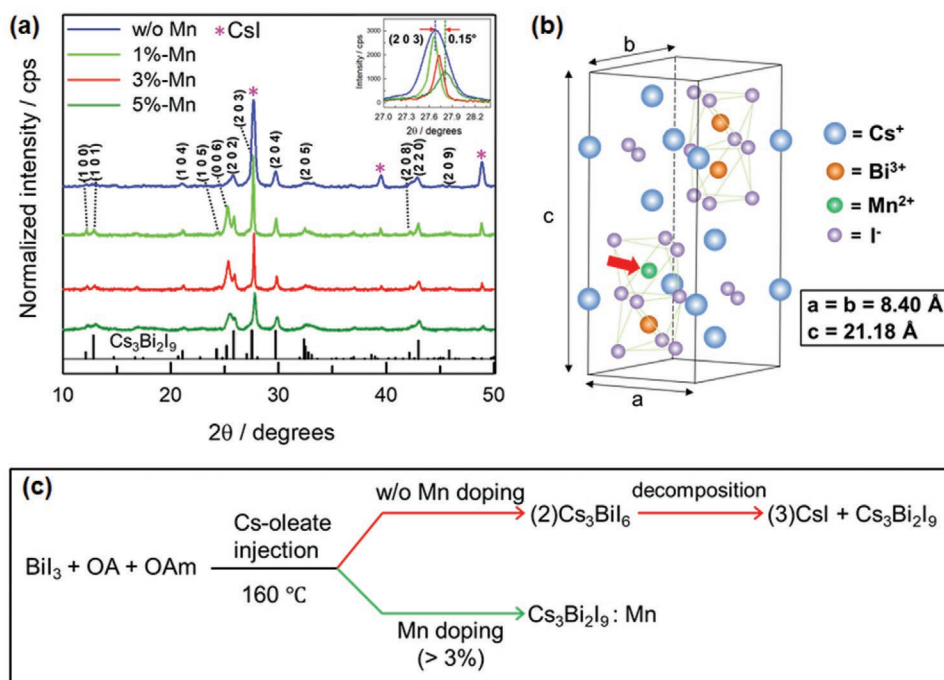


**Figure 1.** a) XRD patterns of the as-prepared Cs<sub>3</sub>Bi<sub>2</sub>I<sub>9</sub> NCs without doping (reference) and with different Mn doping ratios, indexed to a hexagonal crystalline phase with JCPDS reference 01-070-0666 (black line on the bottom), and to a CsI byproduct phase with JCPDS reference 00-006-0311 (pink asterisk) from the ICDD database, respectively. b) Schematic illustration of a unit cell of Cs<sub>3</sub>Bi<sub>2</sub>I<sub>9</sub>:Mn NCs in a 0D dimer structure. The red arrow shows a potential doping position of Mn<sup>2+</sup> ion. c) Proposed synthetic routes of Cs<sub>3</sub>Bi<sub>2</sub>I<sub>9</sub> NCs without and with Mn doping (>3%).

level of the XRD pattern (see Figure S1, Supporting Information), suggesting that a pure phase of Cs<sub>3</sub>Bi<sub>2</sub>I<sub>9</sub>:Mn has been obtained upon a sufficient Mn doping. The XRD data from the Cs<sub>3</sub>Bi<sub>2</sub>I<sub>9</sub>:Mn NCs are well modeled using a structure derived from the 0D dimer structure (see Figure 1b) of Cs<sub>3</sub>Bi<sub>2</sub>I<sub>9</sub> with expanded lattice parameters (see Figure 1b) of Cs<sub>3</sub>Bi<sub>2</sub>I<sub>9</sub> with expanded lattice parameters ( $a = b = 8.40 \text{ \AA}$ ,  $c = 21.18 \text{ \AA}$ ), indicating the formation of a hexagonal crystallographic phase that corresponds to the space group  $P6_3/mmc$  (194), which is in good agreement with previous reported crystals structure of 0D Cs<sub>3</sub>Bi<sub>2</sub>I<sub>9</sub> NCs obtained via the hot injection method upon the injection of TMS-I.<sup>[5]</sup> This suggests that our modified synthetic route can also lead to a pure phase of Cs<sub>3</sub>Bi<sub>2</sub>I<sub>9</sub> NCs (when a sufficient amount of MnI<sub>2</sub> is added to the precursor), while maintaining a safe and low-hazard process. The XRD patterns of the Cs<sub>3</sub>Bi<sub>2</sub>I<sub>9</sub>:Mn NCs show slight and continuous shifts in the peak positions along with the increasing Mn doping ratio (e.g., from 0 to 5%), that is, from 27.60° to 27.75° for the (203) reflection (see the inset in Figure 1a) and from 29.80° to 29.95° for the (204) reflection, indicating a small change in the size of the unit cell dimension. This change is assigned to the partial replacement of the Bi–I bonds with longer bond length ( $\approx 3.10 \text{ \AA}$ )<sup>[31]</sup> by the shorter Mn–I bonds ( $\approx 2.54 \text{ \AA}$ )<sup>[32]</sup> leading to a shrinkage of the unit cell and an upward shift in the  $2\theta$  angles along with more Mn doping, as observed earlier for Mn-doped CsPbCl<sub>3</sub> NCs.<sup>[33]</sup>

To support our hypothesis of Mn doping influencing the formation of Cs–Bi–I NCs, we conducted energy-dispersive X-ray spectroscopy (EDS) measurements for different Cs<sub>3</sub>Bi<sub>2</sub>I<sub>9</sub>:Mn NCs films. The EDS layered images of Cs<sub>3</sub>Bi<sub>2</sub>I<sub>9</sub>:Mn (3%) (Figure S2, Supporting Information) for the compositional elements representatively show the homogeneous elemental

distribution on the surface of the NCs film. The EDS analysis confirms the stoichiometry of Cs<sub>3</sub>Bi<sub>2</sub>I<sub>9</sub>:Mn (0–5%) NCs films in **Table 1**. Interestingly, the Cs<sub>3</sub>Bi<sub>2</sub>I<sub>9</sub> NCs without Mn doping show the expected stoichiometry of Cs<sub>3</sub>BiI<sub>6</sub> that is in fact the mixture of decomposed products, i.e., CsI and Cs<sub>3</sub>Bi<sub>2</sub>I<sub>9</sub> (the molar ratio is 3:1). Upon 1% Mn doping, the relative ratio between Cs and Bi is effectively decreased, meaning that the direct formation of Cs<sub>3</sub>Bi<sub>2</sub>I<sub>9</sub> NCs starts to dominate the overall reaction. With high amounts of Mn doping (e.g., >3%), an exact stoichiometry of Cs<sub>3</sub>Bi<sub>2</sub>I<sub>9</sub> NCs is achieved, which is highly consistent with the findings from the XRD study. The reactivity of the Bi precursor is known to be crucial to obtain different crystal structures of Cs–Bi–I NCs, and it is influenced by the ligand concentration and the reaction temperature.<sup>[7]</sup> Low reactivity of the Bi precursor leads to the formation of Cs<sub>3</sub>BiI<sub>6</sub> (which then decomposes) with a Bi-poor crystal phase, while a high reactivity of the Bi precursor could easily induce the formation of the Bi-rich Cs<sub>3</sub>Bi<sub>2</sub>I<sub>9</sub> phase as the dominant product.

**Table 1.** Elemental analysis (by EDS) for the resultant perovskite NCs without (0%) and with different Mn doping weight ratios. The measured atomic concentration (atom %) for each element is normalized with respect to cesium.

Mn doping ratio	Cs	Bi	I
0%	3.0	1.1	6.0
1%	3.0	1.5	7.5
3%	3.0	1.9	8.8
5%	3.0	2.1	9.1

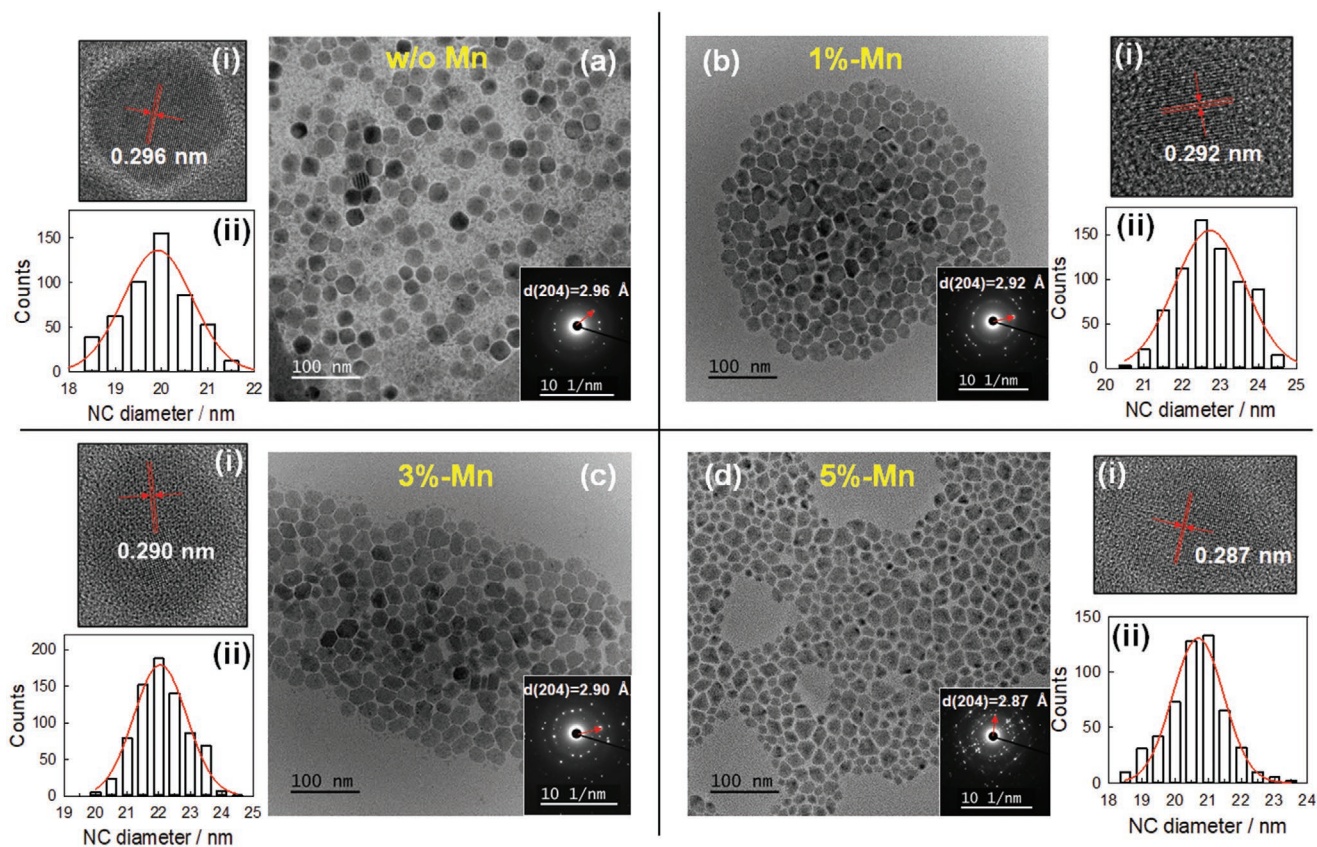


**Figure 2.** TEM images of as-synthesized  $\text{Cs}_3\text{Bi}_2\text{I}_9$  NCs with different Mn doping ratios of a) 0%, b) 1%, c) 3%, and d) 5%. A high-resolution TEM (HRTEM) image of a single  $\text{Cs}_3\text{Bi}_2\text{I}_9$  NC presented in subfigure (i) for respective (a–d), showing clear lattice fringes corresponding to (204) facets. FFT analysis of the HRTEM image is presented in the inset for respective (a–d). The narrow size distribution histogram of the particles is presented in subfigure (ii) for respective (a–d), indicating average diameters of 19.9 nm (0%), 22.7 nm (1%), 22.0 nm (3%), and 20.7 nm (5%) for the cases with different Mn doping ratios, respectively.

In our case, except for the addition of  $\text{Mn}^{2+}$ , the synthesis conditions were identical (e.g., unchanged ligands concentration and reaction temperature), thus, we attribute the promoted synthesis of  $\text{Cs}_3\text{Bi}_2\text{I}_9$  NCs to the enhanced reactivity of the Bi precursor upon the increasing Mn doping (see the proposed synthetic routes of  $\text{Cs}_3\text{Bi}_2\text{I}_9$  NCs in Figure 1c). The underlying mechanism of how Mn doping influences the reactivity of the Bi precursor, plausibly related to the change in the activation energy of the reaction upon the addition of  $\text{Mn}^{2+}$ , remains under investigation.

The influence of Mn doping on the morphology of as-synthesized  $\text{Cs}_3\text{Bi}_2\text{I}_9:\text{Mn}$  NCs was assessed by transmission electron microscopy (TEM). Figure 2a–d shows the shape and size evolution of  $\text{Cs}_3\text{Bi}_2\text{I}_9:\text{Mn}$  NCs with average diameters of 19.9 nm (0% Mn), 22.7 nm (1% Mn), 22.0 nm (3% Mn), and 20.7 nm (5% Mn), respectively. We note that the size distribution of our Mn-doped  $\text{Cs}_3\text{Bi}_2\text{I}_9$  NCs is less than 3 nm, which is much smaller than the reported 9 nm upon a similar synthetic route without Mn-doping.<sup>[27]</sup> This suggests that Mn-doping can effectively narrow the size distribution of the host NCs. The shape of  $\text{Cs}_3\text{Bi}_2\text{I}_9$  NCs without Mn doping is a symmetric hexagon but with rounded edges (Figure 2a), likely attributed to the CsI phase surrounding the as-formed NCs. With 1% and 3% Mn doping (Figure 2b,c), a clear hexagonal shape of  $\text{Cs}_3\text{Bi}_2\text{I}_9:\text{Mn}$  NCs can

be detected with a small size distribution (see subfigure (ii) in Figure 2b,c). This suggests that Mn doping can effectively isolate the as-formed  $\text{Cs}_3\text{Bi}_2\text{I}_9$  NCs compared to the ease of phase aggregation for  $\text{Cs}_3\text{Bi}_2\text{I}_9$  NCs without doping, which has also been observed in the topography comparison of NCs in bulk films (see the SEM images in Figure S3, Supporting Information). Based on the STEM-EDS maps, we confirm that the doped Mn can evenly distribute among the host  $\text{Cs}_3\text{Bi}_2\text{I}_9$  NCs with no observation of a phase separation even at the high doping concentration of 5% (see Figure S4, Supporting Information). Upon rich Mn doping (5%), small hexagonal particles have been observed, mainly attributed to the formation of so-called  $\text{Bi}^0$  seeds during the dissolution of  $\text{BiI}_3$ ,<sup>[27]</sup> whose growth has been inhibited by the excess of  $\text{MnI}_2$  after the injection of Cs-oleate. Based on the HRTEM images of the single  $\text{Cs}_3\text{Bi}_2\text{I}_9:\text{Mn}$  NCs in each case (see subfigures (i) in Figure 2a–d), the lattice distances are 0.296 nm (0% Mn), 0.292 nm (1% Mn), 0.290 nm (3% Mn), and 0.287 nm (5% Mn), respectively, corresponding to the (204) facets, highly consistent with the calculated lattice spacing from the Fast Fourier Transform (FFT) analysis (see the inset in each of Figure 2a–d) of the HRTEM image. This further supports the Mn doping-induced shrinkage of the unit cell observed from the previously discussed XRD data. To explain the overall size and shape evolution of the  $\text{Cs}_3\text{Bi}_2\text{I}_9$  NCs upon

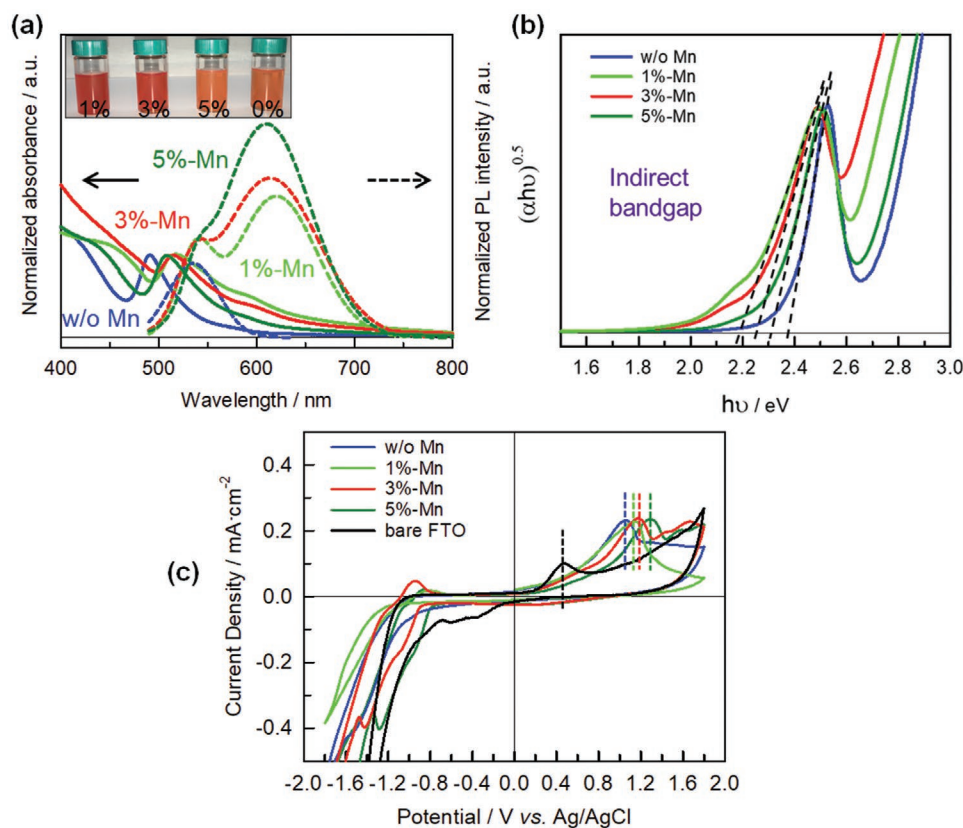


**Figure 3.** a) Absorption spectra (solid lines) and PL spectra (dashed lines) of differently Mn-doped Cs<sub>3</sub>Bi<sub>2</sub>I<sub>9</sub> NCs, respectively. The inset shows the appearance of different Mn-doped Cs<sub>3</sub>Bi<sub>2</sub>I<sub>9</sub> NCs in suspension (color changes from red to orange). b) Tauc plots of steady-state absorption spectra of different Mn-doped Cs<sub>3</sub>Bi<sub>2</sub>I<sub>9</sub> NCs, presenting an indirect bandgap nature. c) Cyclic voltammograms of Cs<sub>3</sub>Bi<sub>2</sub>I<sub>9</sub> NCs films with different Mn doping ratios coated on FTO glasses as WEs in dichloromethane containing 0.1 M Bu<sub>4</sub>NPF<sub>6</sub> as an electrolyte, and bare FTO glass as a reference sample, while Ag/AgCl is the RE and Pt wire is the counter electrode. The voltammograms are recorded with a scan rate of 100 mV s<sup>-1</sup>. The oxidation potential position is highlighted with a dashed line.

different Mn doping, we propose a formation mechanism by combining a classic nucleation theory and growth law<sup>[34]</sup> for conventional semiconductor NCs with a seed-mediated nucleation model for Pb-based perovskite NCs.<sup>[35]</sup> There are two cases for the formation of Cs<sub>3</sub>Bi<sub>2</sub>I<sub>9</sub> NCs depending on the Mn doping amount: i) Comparison of 0% (without doping) and 1%: with the addition of small amounts of Mn<sup>2+</sup>, the nuclei size (Bi<sup>0</sup> seeds) could be effectively enlarged upon the insertion of Mn<sup>2+</sup> in forming larger seeds, that is, Mn:Bi<sup>0</sup>. Thus, under identical reaction times after the injection of Cs-oleate, the Mn:Bi<sup>0</sup> seeds can grow larger compared to Cs<sub>3</sub>Bi<sub>2</sub>I<sub>9</sub> NCs without Mn doping, which was observed in the previous TEM images (Figure 2a,b). ii) Comparison between 1% and 3 & 5% (rich doping): along with the continuous addition of Mn<sup>2+</sup>, although there are relatively more Mn<sup>2+</sup> in the precursor, the excess of Mn<sup>2+</sup> cannot coordinate with Bi<sup>3+</sup> to form Mn:Bi<sup>0</sup> seeds in time due to the high binding energy of Mn–I (267.8 kJ mol<sup>-1</sup>) compared to that of Bi–I (168.2 kJ mol<sup>-1</sup>),<sup>[36]</sup> and the excess of Mn<sup>2+</sup> rather acts as a potential blocking site for monomer attachment for further growth.<sup>[34]</sup> Therefore, the size of the as-formed Cs<sub>3</sub>Bi<sub>2</sub>I<sub>9</sub>:Mn NCs becomes smaller again with increasing Mn doping (see Figure 2c,d). This suggests that Mn doping indeed promotes the synthetic route towards the pure phase of Cs<sub>3</sub>Bi<sub>2</sub>I<sub>9</sub> NCs while modulating their size.

## 2.2. Optical Properties and Band Structures of Cs<sub>3</sub>Bi<sub>2</sub>I<sub>9</sub>:Mn NCs

We now turn to investigate the influence of Mn doping on the optical properties and band structures of the as-formed Cs<sub>3</sub>Bi<sub>2</sub>I<sub>9</sub> NCs. The comparison between the absorption and PL spectra of Cs<sub>3</sub>Bi<sub>2</sub>I<sub>9</sub>:Mn (0–5%) NCs in suspension is shown in Figure 3a. The absorption spectrum of undoped Cs<sub>3</sub>Bi<sub>2</sub>I<sub>9</sub> NCs shows the first excitonic peak at 491 nm with a long tail at lower energies, similarly as in the reported absorption spectra of 0D dimer Cs<sub>3</sub>Bi<sub>2</sub>I<sub>9</sub> NCs.<sup>[5,37]</sup> Upon 1% Mn doping, the absorption spectrum of Cs<sub>3</sub>Bi<sub>2</sub>I<sub>9</sub>:Mn exhibits a clear red-shift compared to that of the undoped NCs, with the first excitonic peak at 517 nm, which also corresponds to the formation of NCs of a larger size, as observed in Figure 2. Upon further Mn doping, the first excitonic peak appears to be blue-shifted to 515 nm (3% Mn) and 508 nm (5% Mn) (see the inset photo in Figure 3a), respectively, indicating a quantum confinement effect induced by increasing the Mn doping in the host Cs<sub>3</sub>Bi<sub>2</sub>I<sub>9</sub> NCs, as also observed for Mn-doped Pb-based perovskite NCs.<sup>[26]</sup> The PL spectrum of Cs<sub>3</sub>Bi<sub>2</sub>I<sub>9</sub> NCs without Mn doping exhibits a big Stokes shift of 44 nm to an emission peak at 535 nm with a full-width-at-half-maximum of 52 nm. After Mn doping of Cs<sub>3</sub>Bi<sub>2</sub>I<sub>9</sub> NCs, a clear dual-emission feature is observed, with one band edge emission of the host NCs centered at about 538 nm and one orange emission from

**Table 2.** Optical and electrochemical data of as-synthesized Cs<sub>3</sub>Bi<sub>2</sub>I<sub>9</sub> NCs with different Mn doping ratios.

Mn doping ratio	$\lambda_{ex}^a$ [nm]	Peak <sub>BE</sub> <sup>b</sup> [nm]	Peak <sub>Mn</sub> <sup>c</sup> [nm]	PLQY [%]	$E_g$ [eV]	$E_{ox}^d$ [V vs Ag/AgCl]	$E_{VB}^e$ [eV]	$E_{CB}^f$ [eV]
0%	491	535	–	0.54	2.38	1.05	5.70	3.32
1%	517	538	620	1.09	2.19	1.15	5.80	3.61
3%	515	537	614	1.23	2.24	1.19	5.84	3.60
5%	508	540	610	1.57	2.31	1.26	5.91	3.60

<sup>a</sup>)First excitonic absorption peak; <sup>b</sup>)Band edge emission peak of host Cs<sub>3</sub>Bi<sub>2</sub>I<sub>9</sub> NCs; <sup>c</sup>)Mn emission peak; <sup>d</sup>) $E_{ox}$  is oxidation potential; <sup>e</sup>)Correlated with the redox potential of Ag/AgCl, converting to  $E_{VB}$ :  $E_{VB} = E_{ox} + 4.65$  eV<sup>[43]</sup>; <sup>f</sup>)Estimated from  $E_{VB}$  and  $E_g$ .

a spin-forbidden  $^4T_1-^6A_1$  Mn d–d transition after the transfer of the exciton energy from the host Cs<sub>3</sub>Bi<sub>2</sub>I<sub>9</sub> to Mn<sup>2+</sup> dopants, as commonly observed for Mn-doped Pb-based perovskite NCs.<sup>[38–40]</sup> Furthermore, the Stokes shift of the band edge emission from the host has been reduced down to the range of 21–32 nm upon Mn doping compared to the case of undoped NCs, meaning that Mn doping can assist in reducing the energy loss for the host NCs in their excited state. We also note that the intensity of the Mn emission gradually increases with more Mn doping amount accompanied by a blue shift in the PL spectra, which is attributed to the increasing Mn–Mn distance and the decreasing effect of Mn–Mn exchange coupling on Mn emission.<sup>[39,28]</sup> The determined PLQYs of Cs<sub>3</sub>Bi<sub>2</sub>I<sub>9</sub>:Mn NCs (Table 2) show a clear enhancement by nearly a factor of 3 after 5% Mn<sup>2+</sup> doping (1.57%) compared to that of the undoped NCs (0.54%), mainly due to the additional PL contribution from the Mn emission. However, the absolute PLQYs are still low (i.e., <2%) as commonly observed for Bi-based perovskite NCs, in relation to their featured direct-indirect transitions.<sup>[10,9]</sup> To confirm the nature of bandgap ( $E_g$ ), we then analyzed the Tauc plots for the absorption spectra of Cs<sub>3</sub>Bi<sub>2</sub>I<sub>9</sub>:Mn NCs (Figure 3b). By setting the exponent factor as 0.5, an indirectly allowed transition feature can be well extracted for all Cs<sub>3</sub>Bi<sub>2</sub>I<sub>9</sub>:Mn (0–5%) NCs, showing a distinguishable influence of Mn doping on the modification of their bandgaps. The extracted  $E_g$  values, along with all key optical data for Cs<sub>3</sub>Bi<sub>2</sub>I<sub>9</sub>:Mn NCs, are summarized in Table 2.

To further clarify the role of Mn doping in tuning the band structure of the host Cs<sub>3</sub>Bi<sub>2</sub>I<sub>9</sub> NCs, electrochemical measurements, that is, cyclic voltammetry,<sup>[41,42]</sup> were conducted. We determined the redox potentials of Cs<sub>3</sub>Bi<sub>2</sub>I<sub>9</sub>:Mn (0–5%) NCs

films on FTO glasses as the working electrodes (WE) in a three-electrode cell system (see details in the Experimental Section). Figure 3c shows the cyclic voltammograms of Cs<sub>3</sub>Bi<sub>2</sub>I<sub>9</sub> NCs films with different Mn doping ratios. The oxidation potential ( $E_{ox}$ ) for each NCs film has been extracted in comparison with that of bare FTO glass (reference) and the values are summarized in Table 2. By correlating the potentials with the redox potential of Ag/AgCl (reference electrode (RE)), the valence bands ( $E_{VB}$ ) of Cs<sub>3</sub>Bi<sub>2</sub>I<sub>9</sub>:Mn NCs (Table 2) can be calculated using the equation " $E_{VB} = E_{ox} + 4.65$  eV".<sup>[43]</sup> Interestingly, we observe the deepening of the  $E_{VB}$  level of the host Cs<sub>3</sub>Bi<sub>2</sub>I<sub>9</sub> NCs along with the increasing Mn doping while no obvious change in the conduction band ( $E_{CB}$ ) level is noticed for NCs with different Mn doping ratios (e.g., 1–5%). Since Mn<sup>2+</sup> ions are known to passivate the surface of perovskite films<sup>[44]</sup> and potentially induce a so-called positive dipole effect,<sup>[45]</sup> we thus attribute the band structure tuning of the host Cs<sub>3</sub>Bi<sub>2</sub>I<sub>9</sub> NCs upon Mn doping to a positive dipole effect triggering the work function shift upwards. This results in the deepening of the  $E_{VB}$  level.

### 2.3. Photophysical Properties of Cs<sub>3</sub>Bi<sub>2</sub>I<sub>9</sub>:Mn NCs

To gain more insights into the exciton recombination dynamics, PL decays of as-formed Cs<sub>3</sub>Bi<sub>2</sub>I<sub>9</sub>:Mn NCs were monitored at 538 nm (emission peak for the host NCs) by conducting time-correlated single-photon counting (TCSPC) measurements in the nanosecond regime (Figure 4a). It has been clearly observed that the increased Mn doping effectively decelerates the excited state decays with an extension of recombination lifetime. All

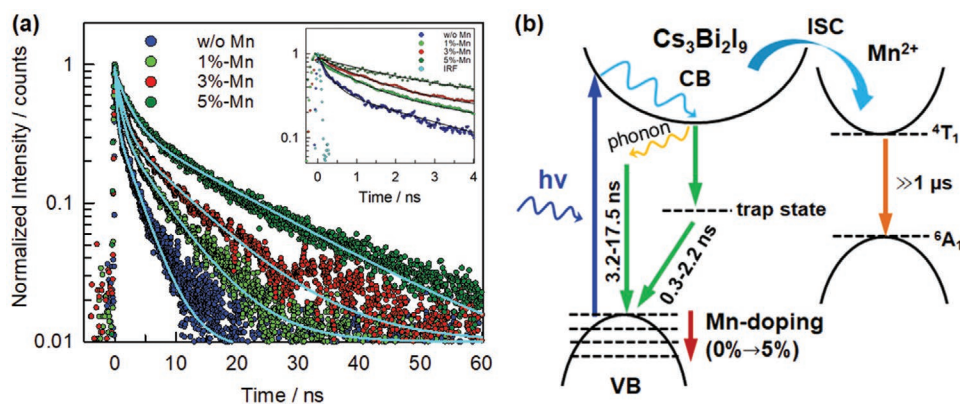


**Figure 4.** a) TCSPC decays of Cs<sub>3</sub>Bi<sub>2</sub>I<sub>9</sub> NCs with different Mn doping ratios in suspension (the inset shows magnified decays in early timescale with an instrument response file), excited at 405 nm, and monitored at 538 nm. Solid lines show the fitting results with a bi-exponential function. b) Scheme for the PL emission mechanisms in Cs<sub>3</sub>Bi<sub>2</sub>I<sub>9</sub>:Mn NCs system. ISC: intersystem crossing; CB: conduction band; VB: valence band.

**Table 3.** Summary of time-resolved PL data of as-synthesized Cs<sub>3</sub>Bi<sub>2</sub>I<sub>9</sub> NCs with different Mn doping ratios.

Mn doping ratio	A <sub>1</sub> [%]	t <sub>1</sub> [ns]	A <sub>2</sub> [%]	t <sub>2</sub> [ns]	t <sub>1/e</sub> <sup>a)</sup> [ns]
0%	61.2	0.30	38.8	3.24	0.67
1%	61.3	0.96	38.7	6.49	1.60
3%	63.2	1.25	36.8	9.97	2.26
5%	58.9	2.20	41.1	17.49	4.29

<sup>a)</sup>Effective lifetime  $t_{1/e}$ , defined as  $I(t_{1/e}) = I(0)/e$ ,  $I(t)$  is the PL intensity as a function of time.

PL decays can be well fitted with a biexponential decay function:  $I(t) = A_1 \times \exp(-t/t_1) + A_2 \times \exp(-t/t_2)$ , which provides two exponential decay constants for all Cs<sub>3</sub>Bi<sub>2</sub>I<sub>9</sub>:Mn (0–5%) NCs, as summarized in Table 3. The fitting results show two components: i) The fast component dominates the overall charge recombination dynamics as its contribution factor is more than 60% on average for all cases (see inset in Figure 4a), and it is assigned to trap-assisted non-radiative recombination, which is either in shallow or deep states ii) The slow component is attributed to the radiative recombination between the band edges with the assistance of phonons due to the nature of indirect transition.<sup>[9]</sup> To simplify the comparison of PL decays, we define an effective lifetime ( $t_{1/e}$ ) with an expression of  $I(t_{1/e}) = I(0)/e$ , where  $I(t)$  is the PL intensity as a function of time.<sup>[46]</sup> We note that the effective lifetime (i.e., 0.67 ns) of the host Cs<sub>3</sub>Bi<sub>2</sub>I<sub>9</sub> NCs without doping has been extended by a factor of more than 6 (i.e., up to 4.29 ns) upon the highest Mn doping concentration (5%), mainly attributed to the passivation effect of Mn doping on the trap states. With respect to the Mn emission dynamics at about 615 nm, we observed extremely long lifetimes ( $\gg 1 \mu\text{s}$ ) for all Mn-doped cases (data are not shown here), which are far beyond the monitoring time range (i.e., up to 1  $\mu\text{s}$ ) of our instrument. The results are consistent with the reported long lifetime (towards millisecond timescale) of Mn emission for doped Pb-based perovskite NCs.<sup>[47,48]</sup>

Based on the band structure characteristics and charge carrier dynamics data, the PL emission model of Cs<sub>3</sub>Bi<sub>2</sub>I<sub>9</sub>:Mn NCs is proposed in Figure 4b. After excitation, there are three relaxation pathways for the excitons at the excited state of the host Cs<sub>3</sub>Bi<sub>2</sub>I<sub>9</sub> NCs: i) radiative recombination of excitons between the ground state and the excited state via the phonon assistance in a recombination lifetime range of 3.2–17.5 ns upon Mn doping (0–5%); ii) a non-radiative relaxation process via trap assistance (either hole traps or electron traps) within a lifetime range of 0.3–2.2 ns that is influenced by Mn doping; iii) a new radiative recombination of excitons via the energy transfer from the excited state of the host Cs<sub>3</sub>Bi<sub>2</sub>I<sub>9</sub> to Mn<sup>2+</sup>. An orange-red light ( $\approx 615 \text{ nm}$ ) is emitted as a result of the Mn doping amount, due to the Mn d-d transition ( ${}^4T_1 \rightarrow {}^6A_1$ ) with an extremely long lifetime towards the millisecond timescale.

#### 2.4. Cs<sub>3</sub>Bi<sub>2</sub>I<sub>9</sub>:Mn NCs-Based Solar Cells

As Mn doping enabled the tuning of the band structure and the photophysical properties of the host Cs<sub>3</sub>Bi<sub>2</sub>I<sub>9</sub> NCs, we expected it to also impact the performance of corresponding solar cells.

Hence, we developed n-i-p planar perovskite solar cell architectures with a light-harvesting layer of Cs<sub>3</sub>Bi<sub>2</sub>I<sub>9</sub>:Mn NCs. The full solar cell structure is FTO/c-TiO<sub>2</sub>/Cs<sub>3</sub>Bi<sub>2</sub>I<sub>9</sub>:Mn NCs/spiro-OMeTAD/Au (see the fabrication details in the Supporting Information), as depicted in Figure 5a. The current density ( $J$ )–voltage ( $V$ ) curves of the best-performing devices based on the Cs<sub>3</sub>Bi<sub>2</sub>I<sub>9</sub>:Mn (0–5%) NCs, recorded under standard 1 Sun illumination (100 mW cm<sup>-2</sup> AM1.5G), are plotted in Figure 5b. Interestingly, a minor hysteresis effect is observed for all the devices, which is insensitive to Mn doping. This phenomenon is consistent with our previous observation for lead-free perovskite NCs-based solar cells compared to conventional lead-based bulk perovskite solar cells,<sup>[30]</sup> attributed to the negligible influence of ion migration under an electric field on the photocurrent flow within the perovskite NCs layer. We note that the short-circuit current densities ( $J_{sc}$ ) in all the cases are quite low (e.g.,  $<0.1 \text{ mA cm}^{-2}$ ), resulting in overall modest power conversion efficiencies (see the performance summary of the best devices in Table S2, Supporting Information). The low  $J_{sc}$  values could be caused by the limited orbital delocalization at the band edges of 0D dimer Cs<sub>3</sub>Bi<sub>2</sub>I<sub>9</sub> NCs (or Mn-doped ones), leading to large exciton-binding energies and relatively poor carrier mobilities.<sup>[5]</sup> However, the  $V_{oc}$  of the best devices has been remarkably improved from 0.58 V for the undoped Cs<sub>3</sub>Bi<sub>2</sub>I<sub>9</sub> NCs-based devices to 0.70 V for the cells containing the 5% Mn-doped Cs<sub>3</sub>Bi<sub>2</sub>I<sub>9</sub> NCs-based absorber. We attribute such an enhancement in  $V_{oc}$  to the deepening of VB level in the host Cs<sub>3</sub>Bi<sub>2</sub>I<sub>9</sub> NCs (see the energy level diagram in Figure 5c) that is induced by Mn doping. Indeed, a deep VB position could provide an enhanced driving force for the splitting of electron (on the conduction band of TiO<sub>2</sub>) and hole (on the valence band of perovskite) quasi-Fermi energy levels actuated by light.<sup>[49–51]</sup>

To further clarify the influence of Mn doping on the charge recombination dynamics in the devices, we conducted transient  $V_{oc}$  decay measurements for all Cs<sub>3</sub>Bi<sub>2</sub>I<sub>9</sub>:Mn NCs-based solar cells at the open-circuit condition after switching off the light irradiation from the solar simulator.<sup>[52]</sup> The results are presented in Figure 5d. The data clearly show that the increase in Mn doping amount effectively decelerates the  $V_{oc}$  decay, which is also in good agreement with the extended excitonic lifetime of the host Cs<sub>3</sub>Bi<sub>2</sub>I<sub>9</sub> NCs upon high Mn doping ratio (Section 2.3). The lifetimes of electrons on the conduction band of TiO<sub>2</sub> can be calculated according to Equation (2)<sup>[53]</sup>

$$\tau_n = -\frac{kT}{e} \left( \frac{dV_{oc}}{dt} \right)^{-1} \quad (2)$$

where  $\tau_n$  is the electron lifetime on the TiO<sub>2</sub> conduction band,  $k$  is the Boltzmann constant,  $T$  is the temperature (K),  $e$  is the elementary charge, and  $t$  is the time after switching off the light irradiation from the solar simulator. Figure 5e presents the estimated electron lifetimes as a function of  $V_{oc}$ , indicating that the electron lifetime is much longer for the devices with a high Mn doping ratio (e.g., 5%) in the higher  $V_{oc}$  region, which is consistent with the  $V_{oc}$  enhancement along with the increasing Mn doping ratio in solar cells. Further engineering should be considered to improve the performance of Cs<sub>3</sub>Bi<sub>2</sub>I<sub>9</sub> NCs-based solar cells, that is, structure engineering (0D dimer to 2D layered structure for Cs<sub>3</sub>Bi<sub>2</sub>I<sub>9</sub> NCs),<sup>[5]</sup> interfacial energy level alignment

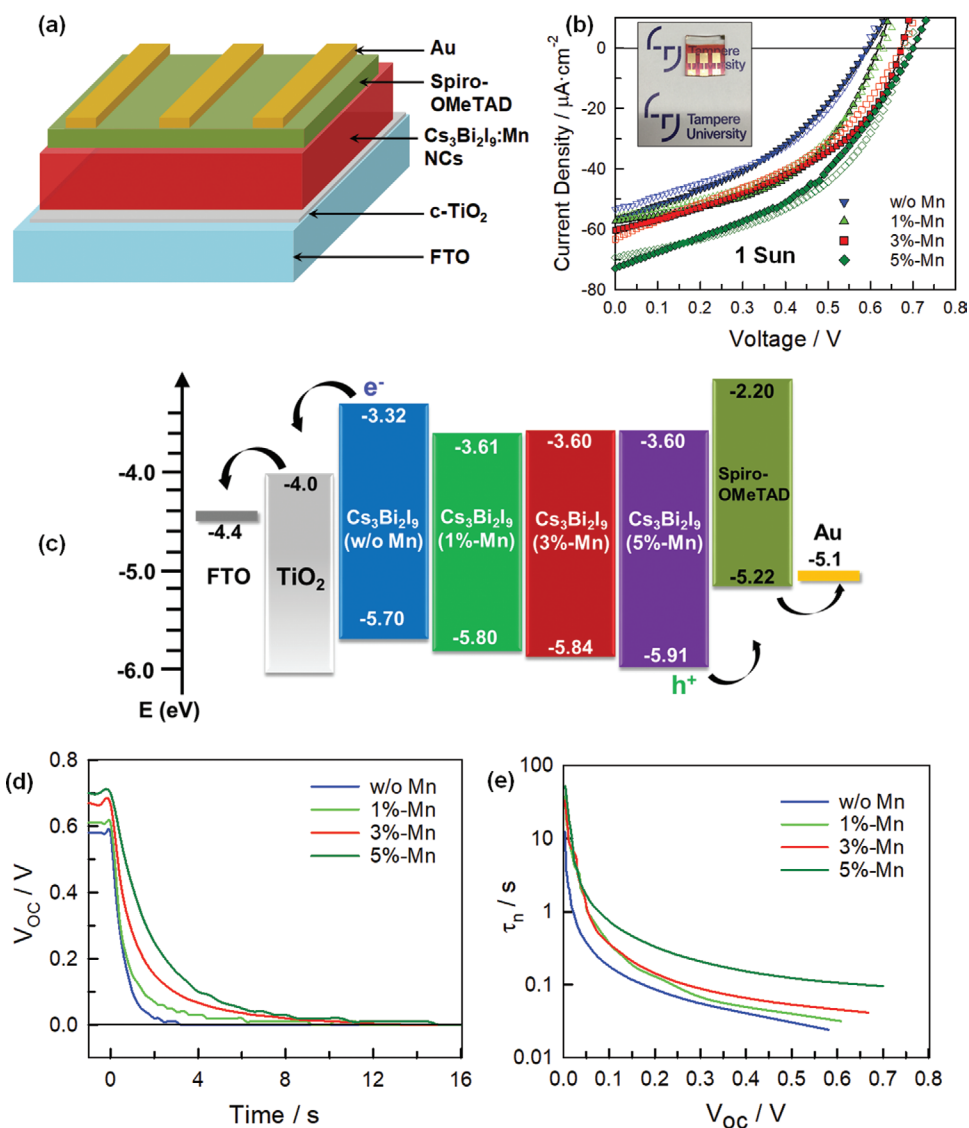


**Figure 5.** a) Architecture of *n-i-p* perovskite NCs-based solar cells in planar structure studied in this work. b) *J-V* curves of the best Cs<sub>3</sub>Bi<sub>2</sub>I<sub>9</sub>:Mn NCs-based solar cells under 1 Sun illumination with a scan rate of 10 mV s<sup>-1</sup> (the symbol with filling presents the forward scan while the symbol with no filling presents the corresponding reverse scan). Inset picture shows the appearance of a typical Cs<sub>3</sub>Bi<sub>2</sub>I<sub>9</sub>:Mn NCs-based solar cell. c) Energy level diagram of Mn-doped Cs<sub>3</sub>Bi<sub>2</sub>I<sub>9</sub> NCs layers and the other constituents of the PSCs considered in this study. The energy levels of each material (except those perovskite NCs) have been taken from the literature.<sup>[54,55]</sup> d) Transient V<sub>oc</sub> decays for different Mn-doped Cs<sub>3</sub>Bi<sub>2</sub>I<sub>9</sub> NCs-based solar cells obtained after turning off the solar simulated light irradiation at *t* = 0. e) Lifetimes of the electrons in the TiO<sub>2</sub> conduction band plotted as a function of the V<sub>oc</sub>.

between perovskite NCs and hole transfer materials, and co-doping engineering for the improvement of charge mobility.

We eventually assessed the long-term stability of as-fabricated Cs<sub>3</sub>Bi<sub>2</sub>I<sub>9</sub>:Mn NCs-based solar cells by storing them in ambient conditions (at 25°C and 40% RH). Figure S5, Supporting Information, presents the comparison of the normalized PCEs of best devices with no Mn doping and with 5% (wt%) Mn doping as a function of storage time. Both devices show highly stable performance (above 95% of their initial PCEs retained after 129 days storage in air), mainly attributed to the high stability (against oxygen and moisture) of the host Cs<sub>3</sub>Bi<sub>2</sub>I<sub>9</sub> NCs. The slight improvement in the stability in Mn-doped devices could be attributed to the surface passivation effect.

### 3. Conclusion

In summary, we have shown that Mn<sup>2+</sup> doping of bismuth-based ternary perovskite NCs (Cs<sub>3</sub>Bi<sub>2</sub>I<sub>9</sub>) promotes their synthesis via a safe and low-hazard hot injection method. In fact, the reactivity of Bi precursor is effectively enhanced upon Mn doping, leading to the pure phase of the targeted Cs<sub>3</sub>Bi<sub>2</sub>I<sub>9</sub> NCs. The size of the host NCs can be tuned by changing the Mn doping concentration, inducing a clear quantum confinement effect. Both the optical and photophysical properties (e.g., PLQY and excitonic lifetime) of the host NCs are improved upon Mn doping due to the reduction of the traps through surface passivation with Mn<sup>2+</sup> ions. Interestingly, we also confirm



the influence of Mn doping on tuning the band structures of the host  $\text{Cs}_3\text{Bi}_2\text{I}_9$ , that is, the deepening of the valence band level with the increase of Mn doping concentration. This corresponds to an enhancement in the  $V_{\text{oc}}$  and the extension of electron lifetime in  $\text{Cs}_3\text{Bi}_2\text{I}_9$ :Mn NCs-based solar cells. This study highlights the important yet still unexplored role of Mn doping in the optimization of the synthetic route of perovskite NCs, in addition to the tailoring of their optoelectronic properties. The application of this approach to other dopants, as well as alternative lead-free perovskite hosts, could enable the facile development of unexplored NC compositions with intriguing properties for future optoelectronic applications.

#### 4. Experimental Section

**Chemicals:**  $\text{Cs}_2\text{CO}_3$  (99.9%),  $\text{BiI}_3$  (99.998%), octadecene (ODE, 90%), oleic acid (OA, 90%), oleylamine (OAm, technical grade, 70%), hexane ( $\geq 95\%$ ), toluene (anhydrous, 99.8%), 2-propanol ( $\geq 99.5\%$ ), tetrabutylammonium hexafluorophosphatetitanium ( $\text{Bu}_4\text{NPF}_6$ , 98%), dichloromethane ( $>99\%$ ), diisopropoxide bis(acetylacetonate) (TDBA) 75 wt.% in isopropanol, bis(trifluoromethane)sulfonimide lithium salt (Li-TFSI, 99.95%), chlorobenzene (extra dry, 99.8%), acetonitrile (99.9%), and 4-tert-butylpyridine (4-tBP) were purchased from Sigma-Aldrich.  $\text{MnI}_2$  (anhydrous,  $>98\%$ ) was obtained from Alfa Aesar. Spiro-OMeTAD (99%) and tris[2-(1H-pyrazol-1-yl)-4-tert-butylpyridine]cobalt(III)tri[bis(trifluoromethane)sulfonimide] (FK209 Co(III),  $>98\%$ ) were purchased from Lumtec and Dyenamo, respectively. All chemicals were used without further purification.

**Preparation of Cs-Oleate:**  $\text{Cs}_2\text{CO}_3$  (0.407 g, 1.25 mmol) was loaded into a 50 mL three-neck flask along with octadecene (ODE, 15 mL) and oleic acid (1.5 mL), degassed under vacuum for 1 h at  $120^\circ\text{C}$ , and then heated under Ar at the same temperature until all  $\text{Cs}_2\text{CO}_3$  was dissolved forming a transparent solution. Since Cs-oleate precipitates out of ODE at room temperature, it needs to be preheated at  $120^\circ\text{C}$  before reaction.

**Synthesis of Mn-Doped  $\text{Cs}_3\text{Bi}_2\text{I}_9$  NCs:** In a modified hot-injection synthesis,<sup>[30]</sup> 58.9 mg of  $\text{BiI}_3$  (0.1 mmol), 7.7 mg (or 15.4 mg, or 30.8 mg) of 0.025 mmol  $\text{MnI}_2$  (or 0.05 mmol, or 0.1 mmol, or 0 mmol for the reference NCs), 4 mL of ODE, 0.5 mL of OA, and 0.5 mL of OAm were loaded into a 25 mL three-neck flask and degassed under vacuum for 1 h at  $120^\circ\text{C}$ . Then, the temperature was increased to  $160^\circ\text{C}$  under Ar and 1 mL of as-prepared Cs-oleate solution (0.075 mmol) was swiftly injected under vigorous stirring. The color of the solution instantaneously turned from transparent orange to dark orange (or bright orange for the reference NCs without Mn doping), exhibiting the formation of NCs. The reaction was kept at the injection temperature for 30 s before an ice-cold water bath was placed under the three-neck flask to quench the further growth of NCs. No additional color change was observed after about 5 s reaction time. The crude solution was then purified with an equal volume of 2-propanol to remove the unreacted precursors and by-products. The resulting turbid mixture was centrifuged at 4500 rpm for 10 min. The resulting perovskite NCs were redispersed in 5 mL hexane and purified again using equal volume of 2-propanol by centrifuging the mixture solution at 3500 rpm for 5 min. Finally, after discarding the supernatant, the resulting NCs were dispersed in desired amount of hexane to tune the concentration for further characterization.

**Electrochemical Measurements:** Cyclic voltammetry of the  $\text{Cs}_3\text{Bi}_2\text{I}_9$  NCs thin films without and with different Mn doping (same process as for cell fabrication) on FTO glass was performed in a reported three-electrode electrochemical cell system using a potentiostat (Ivium Technologies B.V., Compact Stat).<sup>[43]</sup> Experiments were carried out in an electrolyte containing 0.1 M  $\text{Bu}_4\text{NPF}_6$  in dichloromethane. The perovskite NCs thin film sample, a platinum wire, and an Ag/AgCl in saturated KCl were employed as working, counter, and REs, respectively. The area of the WE that was exposed to the electrolyte was  $0.785\text{ cm}^2$ . The measurements were conducted with a scan rate of  $100\text{ mV s}^{-1}$ . A

continuous nitrogen bubbling was applied to the electrolyte during the measurement to minimize the influence of oxygen on the determination of the redox potential. All measured potentials were correlated with the redox potential of Ag/AgCl and converted to energy level (e.g., valence band (VB)) versus vacuum level:  $E_{\text{VB}} = E_{\text{ox}} + 4.65\text{ eV}$ , where  $E_{\text{ox}}$  is the oxidation potential.

**Transient  $V_{\text{oc}}$  Decay Measurements:** The champion perovskite NCs-based solar cells for different cases (reference  $\text{Cs}_3\text{Bi}_2\text{I}_9$  NCs and different Mn-doped  $\text{Cs}_3\text{Bi}_2\text{I}_9$  NCs) were used to measure transient  $V_{\text{oc}}$  decays. The cell was illuminated at open circuit conditions under AM1.5G solar simulated light (one Sun condition,  $100\text{ mW cm}^{-2}$  at  $25 \pm 2^\circ\text{C}$ ) from an AAA-solar simulator (Sciencetech Inc.). After the  $V_{\text{oc}}$  displayed a steady value, the illumination was turned off with a shutter, and the  $V_{\text{oc}}$  decay was monitored using a potentiostat (Ivium Technologies B.V., Compact Stat) with a measurement step of 100–200 ms.

#### Supporting Information

Supporting Information is available from the Wiley Online Library or from the author.

#### Acknowledgements

Dr. Mari Honkanen and Tampere Microscopy Center are gratefully acknowledged for the TEM images. J.H.S., S.Q., P.V., and M.L. acknowledge Jane & Aatos Erkkö foundation (project “ASPIRE”) and Academy of Finland (grant Nos 308307, 319042, and 326461) for financial support. This work is part of the Academy of Finland Flagship Programme, Photonics Research and Innovation (PREIN), Decision No. 320165.

#### Conflict of Interest

The authors declare no conflict of interest.

#### Data Availability Statement

Research data are not shared.

#### Keywords

band structure, lead-free perovskite nanocrystals, manganese doping, time-resolved photoluminescence, transient open-circuit voltage decay

Received: January 7, 2021

Revised: February 17, 2021

Published online: April 1, 2021

- [1] J. Sun, J. Yang, J. I. Lee, J. H. Cho, M. S. Kang, *J. Phys. Chem. Lett.* **2018**, *9*, 1573.
- [2] Q. Fan, G. V. Biesold-McGee, Q. Xu, S. Pan, J. Peng, J. Ma, Z. Lin, *Angew. Chem., Int. Ed.* **2020**, *59*, 1030.
- [3] A. Dey, A. F. Richter, T. Debnath, H. Huang, L. Polavarapu, J. Feldmann, *ACS Nano* **2020**, *14*, 5855.
- [4] T. Cai, W. Shi, S. Hwang, K. Kobbekaduwa, Y. Nagaoka, H. Yang, K. Hills-Kimball, H. Zhu, J. Wang, Z. Wang, Y. Liu, D. Su, J. Gao, O. Chen, *J. Am. Chem. Soc.* **2020**, *142*, 11927.
- [5] S. E. Creutz, H. Liu, M. E. Kaiser, X. Li, D. R. Gamelin, *Chem. Mater.* **2019**, *31*, 4685.

- [6] G. M. Paternò, N. Mishra, A. J. Barker, Z. Dang, G. Lanzani, L. Manna, A. Petrozza, *Adv. Funct. Mater.* **2018**, *29*, 1805299.
- [7] H. Yang, T. Cai, E. Liu, K. Hills-Kimball, J. Gao, O. Chen, *Nano Res.* **2020**, *13*, 282.
- [8] Y. Chen, H. Zeng, P. Ma, G. Chen, J. Jian, X. Sun, X. Li, H. Wang, W. Yin, Q. Jia, G. Zou, *Angew. Chem., Int. Ed.* **2021**, *60*, 2629.
- [9] Y. Zhang, J. Yin, M. R. Parida, G. H. Ahmed, J. Pan, O. M. Bakr, J.-L. Brédas, O. F. Mohammed, *J. Phys. Chem. Lett.* **2017**, *8*, 3173.
- [10] B. Yang, X. Mao, F. Hong, W. Meng, Y. Tang, X. Xia, S. Yang, W. Deng, K. Han, *J. Am. Chem. Soc.* **2018**, *140*, 17001.
- [11] D. J. Norris, N. Yao, F. T. Charnock, T. A. Kennedy, *Nano Lett.* **2001**, *1*, 3.
- [12] D. J. Norris, A. L. Efros, S. C. Erwin, *Science* **2008**, *319*, 1776.
- [13] A. Nag, D. D. Sarma, *J. Phys. Chem. C* **2007**, *111*, 13641.
- [14] R. Beaulac, P. I. Archer, X. Liu, S. Lee, G. M. Salley, M. Dobrowolska, J. K. Furdyna, D. R. Gamelin, *Nano Lett.* **2008**, *8*, 1197.
- [15] B. T. Diroll, G. Nedelcu, M. V. Kovalenko, R. D. Schaller, *Adv. Funct. Mater.* **2017**, *27*, 1606750.
- [16] M. Gong, R. Sakidja, R. Goul, D. Ewing, M. Casper, A. Stramel, A. Elliot, J. Z. Wu, *ACS Nano* **2019**, *13*, 3714.
- [17] S. Das Adhikari, S. K. Dutta, A. Dutta, A. K. Guria, N. Pradhan, *Angew. Chem.* **2017**, *129*, 8872.
- [18] Z. Chen, H. Chen, C. Zhang, L. Chen, Z. Qin, H. Sang, X. Wang, M. Xiao, *Appl. Phys. Lett.* **2019**, *114*, 041902.
- [19] K. Xu, A. Meijerink, *Chem. Mater.* **2018**, *30*, 5346.
- [20] W. Wang, J. Li, G. Duan, H. Zhou, Y. Lu, T. Yan, B. Cao, Z. Liu, *J. Alloys Compd.* **2020**, *821*, 153568.
- [21] H. Liu, Z. Wu, J. Shao, D. Yao, H. Gao, Y. Liu, W. Yu, H. Zhang, B. Yang, *ACS Nano* **2017**, *11*, 2239.
- [22] A. K. Guria, S. K. Dutta, S. Das Adhikari, N. Pradhan, *ACS Energy Lett.* **2017**, *2*, 1014.
- [23] S. Das Adhikari, A. K. Guria, N. Pradhan, *J. Phys. Chem. Lett.* **2019**, *10*, 2250.
- [24] D. Parobek, B. J. Roman, Y. Dong, H. Jin, E. Lee, M. Sheldon, D. H. Son, *Nano Lett.* **2016**, *16*, 7376.
- [25] S. Wang, J. Leng, Y. Yin, J. Liu, K. Wu, S. Jin, *ACS Energy Lett.* **2020**, *5*, 328.
- [26] S. Paul, E. Bladt, A. F. Richter, M. Döblinger, Y. Tong, H. Huang, A. Dey, S. Bals, T. Debnath, L. Polavarapu, J. Feldmann, *Angew. Chem., Int. Ed.* **2020**, *59*, 6794.
- [27] R. D. Nelson, K. Santra, Y. Wang, A. Hadi, J. W. Petrich, M. G. Panthani, *Chem. Commun.* **2018**, *54*, 3640.
- [28] S. Zou, Y. Liu, J. Li, C. Liu, R. Feng, F. Jiang, Y. Li, J. Song, H. Zeng, M. Hong, X. Chen, *J. Am. Chem. Soc.* **2017**, *139*, 11443.
- [29] N. Chen, T. Cai, W. Li, K. Hills-Kimball, H. Yang, M. Que, Y. Nagaoka, Z. Liu, D. Yang, A. Dong, C. Y. Xu, R. Zia, O. Chen, *ACS Appl. Mater. Interfaces* **2019**, *11*, 16855.
- [30] M. Liu, H. Pasanen, H. Ali-Löytty, A. Hiltunen, K. Lahtonen, S. Qudsia, J.-H. Smätt, M. Valden, N. Tkachenko, P. Vivo, *Angew. Chem., Int. Ed.* **2020**, *132*, 22301.
- [31] F. Ma, M. Zhou, Y. Jiao, G. Gao, Y. Gu, A. Bilic, Z. Chen, A. Du, *Sci. Rep.* **2015**, *5*, 17558.
- [32] A. Mackenzie, M. Kolonits, M. Hargittai, *Struct. Chem.* **2000**, *11*, 203.
- [33] S. Das Adhikari, R. K. Behera, S. Bera, N. Pradhan, *J. Phys. Chem. Lett.* **2019**, *10*, 1530.
- [34] J. Y. Rempel, M. G. Bawendi, K. F. Jensen, *J. Am. Chem. Soc.* **2009**, *131*, 4479.
- [35] T. Udayabhaskararao, M. Kazes, L. Houben, H. Lin, D. Oron, *Chem. Mater.* **2017**, *29*, 1302.
- [36] R. B. King, R. H. Crabtree, C. M. Lukehart, D. A. Atwood, R. A. Scott, *Encyclopedia of Inorganic Chemistry*, John Wiley & Sons, Ltd, Chichester, UK **2006**.
- [37] B. Yang, J. Chen, F. Hong, X. Mao, K. Zheng, S. Yang, Y. Li, T. Pullerits, W. Deng, K. Han, *Angew. Chem., Int. Ed.* **2017**, *56*, 12471.
- [38] D. S. Dolzhenkov, C. Wang, Y. Xu, M. G. Kanatzidis, E. A. Weiss, *Chem. Mater.* **2017**, *29*, 7901.
- [39] T. Qiao, D. Parobek, Y. Dong, E. Ha, D. H. Son, *Nanoscale* **2019**, *11*, 5247.
- [40] M. Liu, G. K. Grandhi, S. Matta, K. Mokurala, A. Litvin, S. Russo, P. Vivo, *Adv. Photonics Res.* **2021**, *2*, 2000118.
- [41] G. F. Samu, R. A. Scheidt, P. V. Kamat, C. Janáky, *Chem. Mater.* **2018**, *30*, 561.
- [42] L. Canil, T. Cramer, B. Fraboni, D. Ricciarelli, D. Meggiolaro, A. Singh, M. Liu, M. Rusu, C. M. Wolff, N. Phung, Q. Wang, D. Neher, T. Unold, P. Vivo, A. Gagliardi, F. De Angelis, A. Abate, *Energy Environ. Sci.* **2021**, *14*, 1429.
- [43] M. Liu, S. Makuta, S. Tsuda, S. Russo, S. Seki, J. Terao, Y. Tachibana, *J. Phys. Chem. C* **2017**, *121*, 25672.
- [44] W. J. Mir, A. Swarnkar, A. Nag, *Nanoscale* **2019**, *11*, 4278.
- [45] K. Choi, J. Lee, H. Il Kim, C. W. Park, G. W. Kim, H. Choi, S. Park, S. A. Park, T. Park, *Energy Environ. Sci.* **2018**, *11*, 3238.
- [46] M. Liu, M. Endo, A. Shimazaki, A. Wakamiya, Y. Tachibana, *ACS Appl. Energy Mater.* **2018**, *1*, 3722.
- [47] J. Ghosh, M. Hossain, P. K. Giri, *J. Colloid Interface Sci.* **2020**, *564*, 357.
- [48] K. Xing, X. Yuan, Y. Wang, J. Li, Y. Wang, Y. Fan, L. Yuan, K. Li, Z. Wu, H. Li, J. Zhao, *J. Phys. Chem. Lett.* **2019**, *10*, 4177.
- [49] W. Shockley, H. J. Queisser, *J. Appl. Phys.* **1961**, *32*, 510.
- [50] N. K. Elumalai, A. Uddin, *Energy Environ. Sci.* **2016**, *9*, 391.
- [51] X. Xu, L. Xiao, J. Zhao, B. Pan, J. Li, W. Liao, R. Xiong, G. Zou, *Angew. Chem., Int. Ed.* **2020**, *59*, 19974.
- [52] S. K. Matta, K. Kakiage, S. Makuta, A. Veamatahau, Y. Aoyama, T. Yano, M. Hanaya, Y. Tachibana, *J. Phys. Chem. C* **2014**, *118*, 28425.
- [53] A. Zaban, M. Greenshtein, J. Bisquert, *ChemPhysChem* **2003**, *4*, 859.
- [54] H.-S. Kim, C.-R. Lee, J.-H. Im, K.-B. Lee, T. Moehl, A. Marchioro, S.-J. Moon, R. Humphry-Baker, J.-H. Yum, J. E. Moser, M. Grätzel, N.-G. Park, *Sci. Rep.* **2012**, *2*, 591.
- [55] H. Zhang, M. Liu, W. Yang, L. Judin, T. I. Hukka, A. Priimagi, Z. Deng, P. Vivo, *Adv. Mater. Interfaces* **2019**, *6*, 1901036.